Available online at www.sciencedirect.com
ScienceDirect
Trans. Nonferrous Met. Soc. China 33(2023) 3348−3363
Transactions of Nonferrous Metals Society of China
www.tnmsc.cn

Mechanical properties anisotropy of Ti−6Al−4V alloy fabricated by β forging

Han-bo WENG[1,2], Sen-sen HUANG[2], Jie YANG[2,3], Min QI[2,3], Ying-jie MA[2,3], Yu-xiang WANG[2], Dao-kui XU[2,3], Jian-ke QIU[2,3], Jia-feng LEI[2,3], Bin GONG[1], Rui YANG[2,3]

1. College of Mechanical and Power Engineering, Shenyang University of Chemical Technology, Shenyang 110142, China;
2. Shi-changxu Innovation Center for Advanced Materials, Institute of Metal Research, Chinese Academy of Sciences, Shenyang 110016, China;
3. School of Materials Science and Engineering, University of Science and Technology of China, Shenyang 110016, China

Received 23 March 2022; accepted 31 May 2022

Abstract: The anisotropy of tensile properties and fracture toughness of Ti−6Al−4V (Ti64) alloy fabricated by β forging was investigated. In order to evaluate anisotropic mechanical properties, the microstructure and crystallographic texture of billets with different orientations were characterized, and the influence of sampling direction on tensile properties and fracture toughness was studied. The results reveal that the prior β grains of Ti64 billet display pan-cake-type characteristics. At room temperature, the alloy is mainly composed of α phase, and several α phase variants produced by $\beta\rightarrow\alpha$ phase transformation decrease the α texture intensity. The anisotropy of mechanical properties is affected by prior β grain morphology and the slip activation related to α texture. The initiation toughness was obtained by the *J*-integral resistance curve method. The initiation toughness was divided into intrinsic and extrinsic toughness by calculation. The anisotropy of intrinsic toughness is mainly attributed to the size of crack tip plastic zone, which is affected by prior β grain morphology. In contrast, the extrinsic toughness is affected by zigzag degree of crack, which is mainly influenced by α lamellae and colonies.

Key words: titanium alloy; β forging; texture; *J*-integral; fracture mechanism; anisotropy

1 Introduction

Titanium alloys have excellent comprehensive properties, such as high specific strength, favorable fracture toughness and outstanding corrosion resistance. Thus, they have been widely used in aerospace and marine fields [1−4]. Currently, the criteria for evaluating structural materials have changed from the principle of fail-safe design to damage tolerance design [5]. Compared with the near-α and α titanium alloys, the $\alpha+\beta$ and near-β titanium alloys show better strength and toughness matching. The fracture toughness of titanium alloy depends on several factors, such as microstructure [6−12], additive elements [13−15], texture [16], back stress between different phases [17−19] and slipping deformation [20]. It has been proven that the fracture toughness of lamellar structure is higher than those of bimodal and equiaxed structures. The characteristics of lamellar structure, such as α lamellae [10], grain boundary α and α colonies [21,22] also influence fracture toughness. Owing to the lamellar structure precipitated after the β phase processing [23], β heat-treatment or β thermal deformation is usually

Corresponding author: Ying-jie MA, Tel: +86-24-83978025, E-mail: yjma@imr.ac.cn;
Sen-sen HUANG, Tel: +86-24-83978025, E-mail: sshuang13s@imr.ac.cn
DOI: 10.1016/S1003-6326(23)66338-1

carried out to improve the fracture toughness and impact properties. However, the anisotropy of mechanical properties is induced due to β phase processing. Nonetheless, the structural component endures the load from different directions under the actual service condition. Therefore, investigating anisotropic mechanical properties is necessary for the reliability evaluation.

According to the literature, the anisotropy is partly affected by the texture formation after β thermal deformation. Moreover, as the forging reduction increases, the (0002) plane of primary α rotates and the intensity of the texture decreases [24]. The {001} β texture is suppressed by the precipitation of α phase [25], which weakens the anisotropy. Moreover, the *c*-axis of α texture is perpendicular to the crack propagation direction and the crack plane, resulting in the highest fracture toughness [16]. The anisotropy in fracture toughness of metastable β titanium alloys is attributed to β texture and the crack propagates along the precipitation free zone [26]. Nevertheless, as a type of $\alpha+\beta$ titanium alloy, the previous experiments were primarily used to obtain plane stress−strain fracture toughness due to its medium strength and high fracture toughness (K_Q). Notably, the thickness of the specimen significantly influences the assessment of K_Q. Thus, K_Q could not accurately reflect the characteristics of fracture toughness. Furthermore, the effect of β texture on the anisotropy of Ti64 alloy is weakened due to the precipitation of α lamellae from prior β grains. However, the mechanical properties anisotropy of the billet was still apparent. For the relationships between their microstructure features and properties of different orientations, no relevant research work could be directly referred to. Moreover, the underlying anisotropy toughening mechanisms have not been presented in detail.

The initiation toughening mechanism of different alloys can be divided into two types, intrinsic toughening and extrinsic toughening [27]. Intrinsic toughening is dominated by the physical properties of the materials [28,29], while extrinsic toughening is dominated by fracture mechanisms [30,31]. However, the anisotropy based on intrinsic and extrinsic toughness has rarely been investigated. Moreover, to better comprehend and quantify the crack propagation process, the energy conditions that govern the fracture process, including initiation and propagation toughness, should also be investigated. However, most studies on fracture toughness of titanium alloys focused on fracture initiation toughness (K_Q/K_{IC}).

This study systematically investigated the tensile properties and fracture toughness anisotropy of $\alpha+\beta$ Ti64 alloy. The yield strength and elongation anisotropy were analyzed by prior β grain morphology and α texture. Furthermore, tests were carried out via the *J*-integral approach to solve the K_Q that could not meet the plane strain requirement. Meanwhile, the plane strain initiation toughness (K_{JIC}) and the propagation toughness (K_{SS}) were obtained simultaneously. Further, the quantitative calculation was used to subdivide initiation toughness into intrinsic and extrinsic toughness to understand the fracture mechanism of different orientations. Thus, the factors affecting fracture toughness anisotropy were further revealed accurately.

2 Experimental

2.1 Material preparation

The chemical composition of provided Ti64 alloy is listed in Table 1. The β transus temperature was (975±5) °C, determined by the metallographic analysis method. The dimensions of the original bar were *d*200 mm × 200 mm. The bar was kept at 1030 °C (β phase field) for 1.5 h and subsequently forged with 60% deformation reduction. The forging direction is the axial direction (AD) as shown in Fig. 1(a). Then, the billet with dimensions of *d*280 mm × 80 mm was obtained. In order to eliminate residual stress, the billet was annealed at 750 °C ($\alpha+\beta$ phase field) for 4 h followed by air cooling. The heat-treated billet was used for the following study.

Table 1 Chemical composition of Ti64 billet

Al	V	Fe	C	H	O	N	Si	Ti
6.47	4.29	0.24	0.02	0.0016	0.16	0.0036	0.01	Bal.

2.2 Tensile properties measurement

The orientation of tensile test specimens obtained from the billet is shown in Fig. 1(a). Based on the orientation of the tensile specimens, the orientations are named radial direction (RD) and AD. Cylindrical dog-bone-shaped tensile specimens

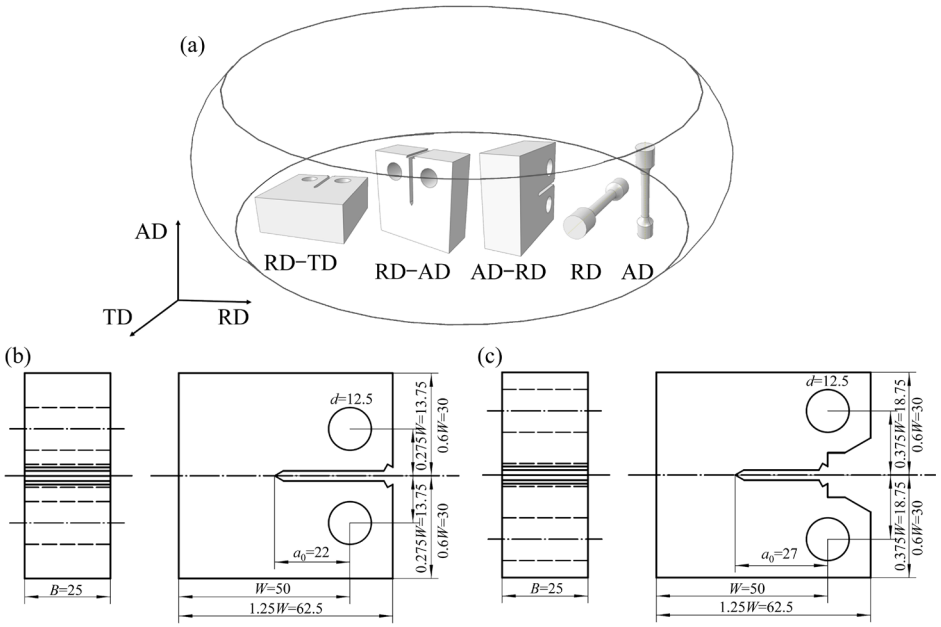

Fig. 1 Orientations of CT and tensile specimens (a), size of K_{IC} specimens (b), and size of J_{IC} specimens (c) (Unit: mm)

with a length of 60 mm and a radius of 5 mm were selected. The tensile tests were carried out on a universal testing machine (TSE504D) with a rate of 0.5 mm/min at ambient temperature in order to obtain yield strength (YS), ultimate tensile strength (UTS), and elongation (EL). At least six specimens in RD along the thickness and at least three specimens in AD were used to ensure the reliability of the data. Eventually, the elasticity modulus (E) of different orientations was measured by the resonant method.

2.3 Fracture toughness test

The K_{IC} test was performed to determine plane strain fracture toughness. For ductile fracture, plastic deformation dominantly occurs at crack tips. Therefore, fracture toughness is usually described in the form of a J-integral resistance curve [32]. The K_{IC} test was performed in accordance with ASTM E399 [33], and the J_{IC} test followed ASTM 1820 [34]. The compact tension (CT) specimens in three orientations RD−TD, AD−RD and RD−AD selected for the tests are shown in Fig. 1(a). The K_{IC} and J_{IC} specimens were machined with the dimensions shown in Figs. 1(b) and (c), respectively. The dimensions of thickness (B), width (W), and the mechanical notch length a_0 are marked in the figures. The K_{IC} test was carried out first, and then the J_{IC} test was carried out later. The thickness of the CT specimens selected was B=25 mm, and the corresponding width was W=50 mm for both K_{IC} and J_{IC} tests. The initial crack length was a_0=22 mm for K_{IC} test and a_0=27 mm for J_{IC} test. The prefabricated fatigue crack was introduced at ΔK=20 MPa·m$^{1/2}$. In order to meet the requirements of $0.45W \le a \le 0.55W$ in K_{IC} test and $0.45W \le a \le 0.7W$ in J_{IC} test, the length of prefabricated crack was selected to be 3 mm. The tests were operated using a fatigue testing system (MTS 809), while the pre-cracked specimens were stretched to break with a rate of 0.5 kN/s for K_{IC} test. The cracks propagated to a certain length with a rate of 1 mm/min for J_{IC} test. Subsequently, the curves of crack opening displacement and load were plotted, and the values of P_Q and P_{max} were obtained from the curves. The P_Q was obtained by 95% slope intersection, and P_{max} was acquired from the maximum of the force. After the experimental calculation of K_Q, the plane strain fracture toughness needs to be verified. The quantitative verification can be carried out by using Eqs. (1) and (2) [35]:

$$\frac{P_{max}}{P_Q} < 1.1 \tag{1}$$

$$B, a, (W-a) > 2.5\left(\frac{K_{IC}}{YS}\right)^2 \tag{2}$$

However, the K_Q obtained from experiments does not meet the requirements mentioned above.

Although the plane strain requirement was not satisfied, it was required to analyze the crack propagation using K_Q specimens. Furthermore, the J_{IC} test was required to be conducted, which required a smaller specimen size. For the J_{IC} test, the multi-specimen method was adopted, which involved at least five valid specimens. The experiments were analyzed by the curves of crack tip opening displacement (CTOD) versus load, which contained plastic and elastic parts. Equations (3) and (4) were used to calculate K_Q, where $P_{(i)}=P_Q$, $a_i=a_0$. Equations (3)−(8) were used to calculate J_Q.

$$K_{(i)}=\frac{P_{(i)}}{(BB_N W)^{1/2}}f\left(\frac{a_i}{W}\right) \tag{3}$$

$$f\left(\frac{a_i}{W}\right)=\left\{\left(2+\frac{a_i}{W}\right)\left[0.866+4.64\frac{a_i}{W}-13.32\left(\frac{a_i}{W}\right)^2+14.72\left(\frac{a_i}{W}\right)^3-5.6\left(\frac{a_i}{W}\right)^4\right]\right\}\Bigg/\left(1-\frac{a_i}{W}\right)^{3/2} \tag{4}$$

where $K_{(i)}$ is the linear-elastic stress intensity factor, $P_{(i)}$ is the ultimate load, B_N is the thickness of specimens excluding grooves, and a_i denotes the total crack length of each specimen after the test. For the K_{IC} specimens, the specimens had no side grooves, while for the J_{IC} specimens, they had side grooves after prefabricating the crack.

$$J=J_{el}+J_{pl}=\frac{K_{(i)}^2}{E'}+J_{pl} \tag{5}$$

where J is the J-integral value, J_{el} and J_{pl} denote the elastic and plastic components of J-integral, respectively and $E'=E$ in plane stress or $E'=E/(1-\mu^2)$ in plane strain (μ is the Poisson's ratio).

$$J_{pl}=\frac{\eta_{pl}A_{pl}}{B_N b_0} \tag{6}$$

where A_{pl} is the plastic zone area of each load−displacement curve, $\eta_{pl}(=2+0.522b_0/W)$ is the load-line displacement is used for A_{pl}, and $b_0(=W-a_0)$ [34] is the initial ligament length. The J-integral value calculated from Eqs. (3)−(7) should be corrected for crack growth.

$$J=J_{el}+\frac{J_{pl}}{1+\left(\frac{\alpha-0.5}{\alpha+0.5}\right)\frac{\Delta a}{b_0}} \tag{7}$$

where α=0.9 for CT specimen.

$$\Delta a=a-a_0 \tag{8}$$

where Δa is the increment of crack propagation. The Δa values of each specimen are determined by averaging the measured values of nine points within the thickness span. Before stretching to fracture, it is required to oxidize the specimens at 500 °C for 1 h additionally in order to measure Δa. Then, the J-integral versus crack propagation for CT specimens can be recorded. After calculation and measurement, a point is assigned for each sample. Then, a J-integral curve is fitted according to these points. The equation of the fitting curve is as follows: $J=C_1\Delta a^{C_2}$ (C_1 is the scaling constant, and C_2 is the the toughening index). The points on the curve need to meet specific requirements before proceeding to the next step. The construction line is determined according to the equation: $J=2\sigma_Y\Delta a$, σ_Y=(YS+UTS)/2. Built the construction line, and then plot a deviation line parallel to the construction line intersecting the abscissa at 0.2 mm. The intersection of the 0.2 mm deviation line and the fitting curve is determined as J_Q (J_Q is the provisional J-integral values). Eventually, J_Q is equivalent to J_{IC} only if the following equations Eqs. (9) and (10) are satisfied:

$$B\geq 10J_Q/\sigma_Y \tag{9}$$

$$b_0\geq 10J_Q/\sigma_Y \tag{10}$$

2.4 Microstructure and fracture surface characterization

The specimens for metallographic structure observation were prepared by mechanical grinding, polishing, and etching for about 5 s. The etching reagent consisted of 3 vol.% HF, 3 vol.% HNO_3, and 94 vol.% H_2O. The orientations of the metallographic were extracted from RD−AD and RD−TD planes, and the observation was carried out by optical microscopy (OM, Axiovert 200 MAT) and scanning electron microscope (SEM, MIRA3). The electron backscatter diffraction (EBSD, NordlysMax3) was carried out at a step size of 6 μm, and the data were analyzed with Channel 5 software. The reconstruction β phase was calculated by MATLAB with the MTEX toolbox [36]. Calculations were carried out following the procedure mentioned in the phase transition section of the parent β phase reconstruction in titanium

alloys. The computations are based on the Burgers orientation relationship that aligns (110) plane of the β phase with the (0001) plane of the α phase and the $[1\bar{1}1]$ direction of the β phase with the [2110] direction of the α phase. The cross-section was taken from the center of the K_Q specimens in order to analyze the crack zigzag degree. The cross-section and the macroscopic appearance of the fracture surface were photographed using a digital microscope (DM, VHX−1000). Moreover, the fracture surfaces of the tensile specimens and the K_Q specimens were characterized by SEM.

3 Results and discussion

3.1 Microstructure

Figures 2(a) and (b) exhibit the microstructure of Ti64 billet. The microstructure shows an elongated prior β grain morphology with narrow width and relatively zigzag prior β grain boundaries. The elongated prior β grains are the contributory cause of mechanical properties anisotropy [26]. A typical lamellar structure is demonstrated at high magnification, as shown in Figs. 2(c) and (d). The β lamellae are arranged vertically or deflected at an angle on both sides of the grain boundary. The β phases are joined together and arranged in neat rows. Moreover, little difference is observed at grain boundary between different orientations.

Figure 3 shows α texture and reconstructed β texture of Ti64 alloy, which exhibits that the α texture is $\langle 0001\rangle$//RD and $\langle 11\bar{2}0\rangle$//AD. Moreover, there exists a variant selection phenomenon of transition from β phase to α phase. When adjacent prior β grains have a common $\langle 110\rangle$ orientation, the c-axis of the secondary α phase precipitated on both sides of the grain boundary are along this common $\langle 110\rangle$ orientation, which results in α texture in β forging billet [35]. Therefore, the intensity of the original β texture is higher than that of the reconstructed β texture.

3.2 Tensile properties

The tensile properties of Ti64 billet in RD and AD are presented in Table 2. Furthermore, Fig. 4 exhibits the engineering stress−strain curves at different orientations. The curves clearly illustrate the difference between the tensile properties corresponding to RD and AD. RD exhibits higher YS (861 MPa) and EL (8.9%) than those in AD. The anisotropy of UTS is unapparent. However, UTS in RD is still slightly larger than that in AD.

The RD specimen consists of many elongated prior β grains on cross-section parallel to the fracture surface, as shown in Fig. 2(b). Compared with large equiaxed prior β grains in AD specimen,

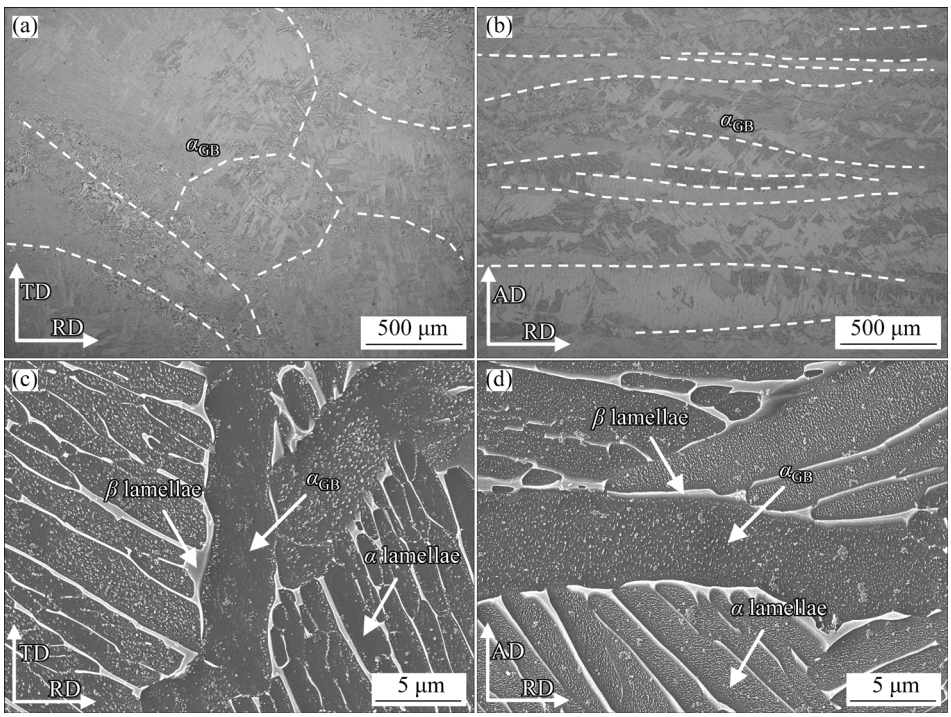

Fig. 2 Prior β grain morphology in different planes: (a) RD−TD plane; (b) RD−AD plane; β lamellae near grain boundary of α in different planes: (c) RD−TD plane; (d) RD−AD plane (The dotted line represents the interface of adjacent prior β grains)

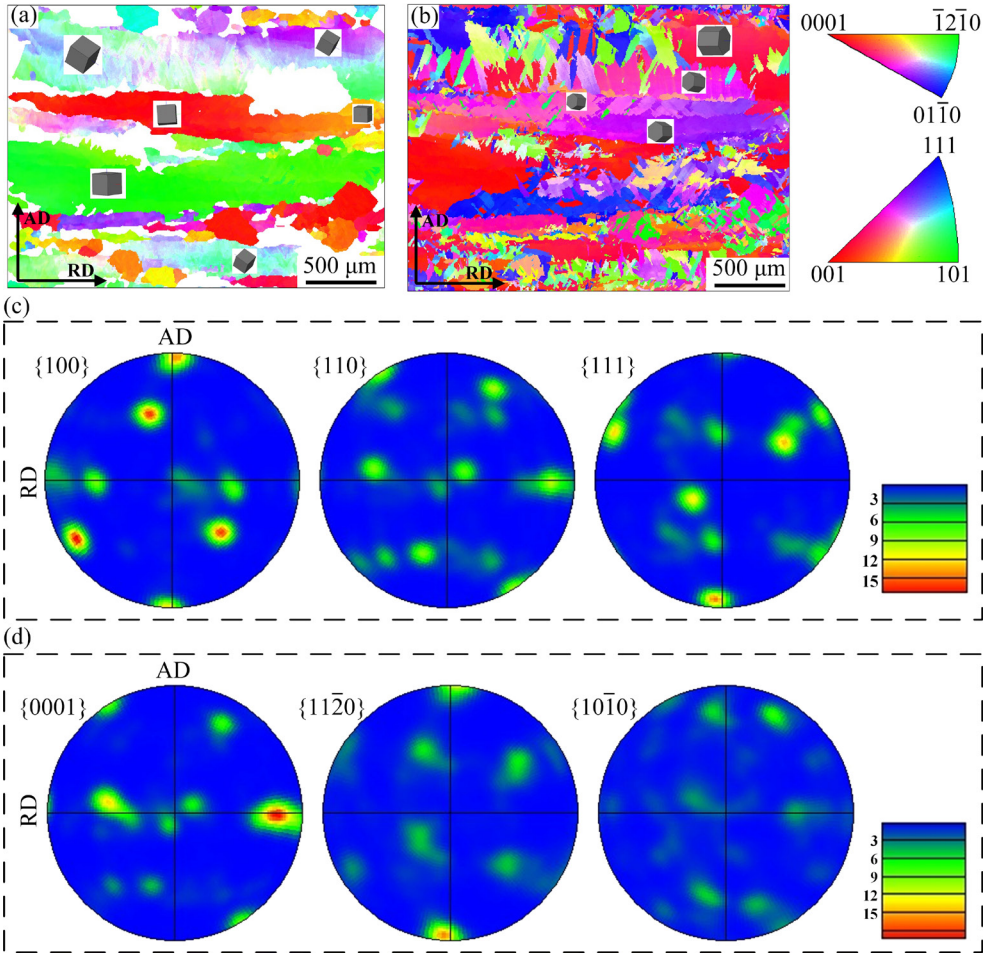

Fig. 3 Inverse pole figure (IPF) map (a) and pole figure (c) of reconstructed β phase in RD−AD plane, and IPF map (b) and pole figure (d) of α phase in RD−AD plane

Table 2 Tensile properties with different orientations

Tensile orientation	YS/MPa	UTS/MPa	EL/%
RD	861±14	935±16	8.9±2.1
AD	780±15	914±9	7.7±2.3

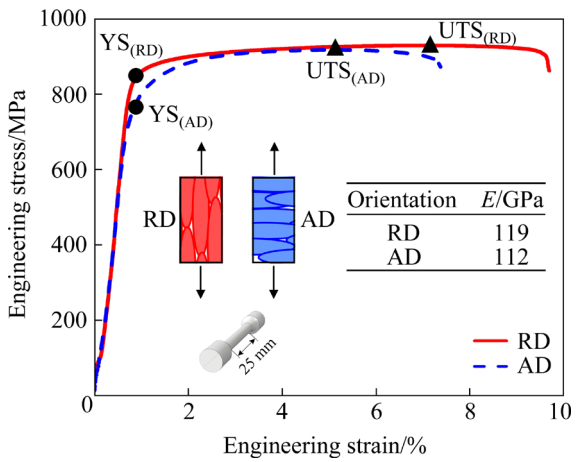

Fig. 4 Engineering stress−strain curves with different tensile orientations

as shown in Fig. 2(a), the number of prior β grains in RD is significantly larger than that in AD. The phenomenon conforms to the Hall−Petch relationship, which results in higher YS in RD specimens [6]. Figure 5(a) displays the IPF map of three orientations. Figure 5(b) shows Schmid factor (SF) contour map for different slip systems. The critical shear stress of the $\langle c+a \rangle$ slip system is extremely high. Thus, it is extremely difficult to be activated in the process of tensile testing at ambient temperature. The critical shear stress of basal plane slip is larger than that of prismatic slip. Thus, the probability of basal plane slip is low. Comparative analysis of Figs. 5(a) and (b) shows that the texture $\langle 11\bar{2}0 \rangle$//AD promotes prismatic slip with SF of 0.45. Figures 5(c)−(e) exhibit the SF distribution of prismatic slip along RD and AD. The SF of AD is 0.4, which accounts for 67.9% of the total prismatic slip. For RD, it is only 24.4%. Thus, it can be concluded that texture decreases YS in AD.

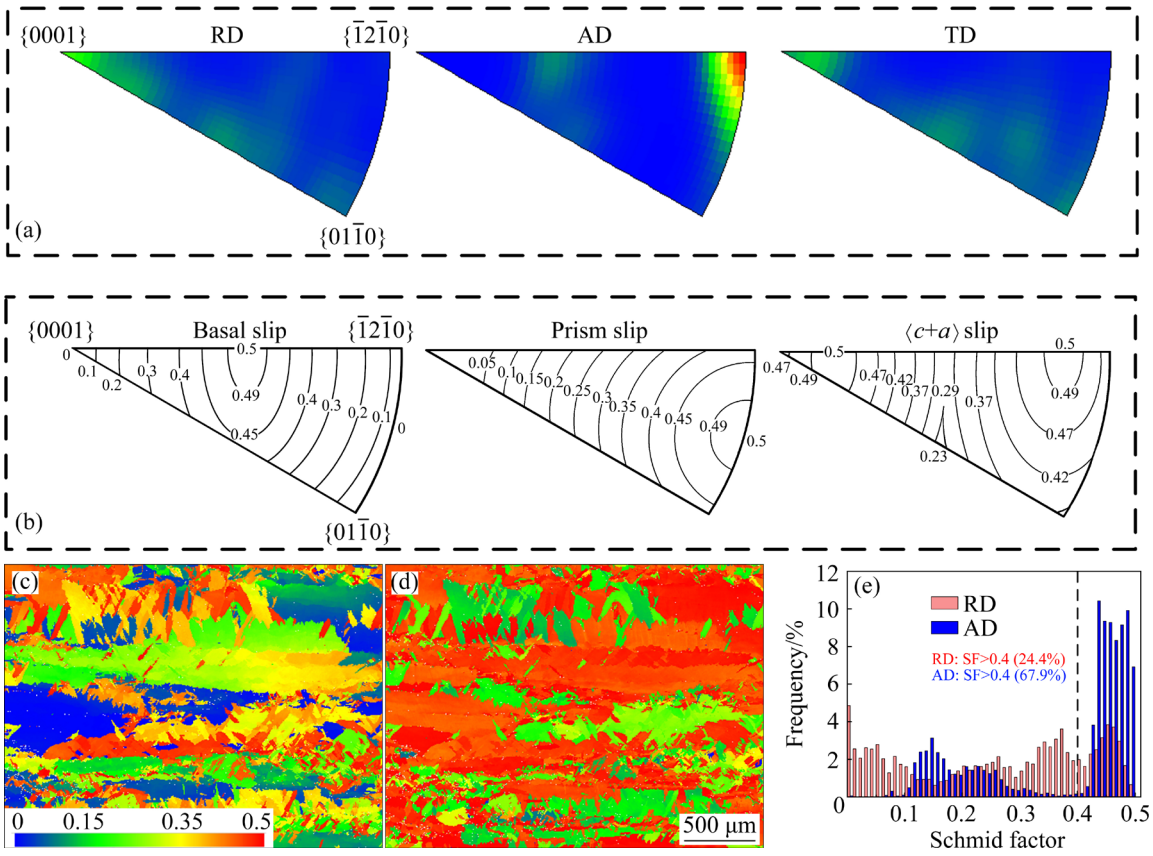

Fig. 5 IPF map of α phase with different orientations (a), SF contour maps of α phase with different slip systems (b), SF map of prismatic slip in RD (c), SF map of prismatic slip in AD (d), and quantitative statistics of SF distribution with prismatic slip (e)

However, the EL in AD is lower than that in RD, which could be explained by the anisotropy being dominated by elongated prior β grains. According to the previous studies, the tensile ductility is determined by the shear stress direction and the grain boundary effective slip length [37]. In this experiment, the effective slip lengths of RD and AD are consistent. Nevertheless, AD loading leads to linear propagation of cracks after crack nucleation, resulting in the reduction of EL in AD. This phenomenon can be verified by the fracture surface and the cross-section perpendicular to the fracture surface of the tensile specimens.

Figure 6 presents the tensile fracture surfaces of Ti64 alloy in RD and AD. Figures 6(a)−(c) demonstrate a rough fracture surface consisting of several cleavage facets, tearing ridges and dimples, which is consistent with the results reported in previous studies [38]. Figures 6(d)−(f) illustrate that the fracture surface of AD specimens is mainly dominated by several steps and facets. The formation mechanism of the steps originates from void and microcrack at lamellae junction or grain boundary. Figures 6(d)−(f) illustrate many flat facets, which is due to the normal stress being perpendicular to the long axis of prior β grains. The crack propagates easily after nucleation, which is related to low EL of AD. Furthermore, the fracture surface illustrates that RD has more prior β grains than AD. The phenomenon proves that the prior β grain size of cross-section and the YS meet the Hall−Patch relationship. Figures 7(a) and (b) show cross-sections perpendicular to the fracture surface of the RD and AD tensile specimens, respectively. The cracks pass through massive prior β grains for RD specimens, which results in significant deflection of the crack. While for AD specimens, most of the cracks propagate horizontally inside the prior β grains, and a small portion of the cracks may propagate along the colony boundaries. Consequently, the anisotropy of tensile properties is mainly controlled by prior β grain morphology and then influenced by α texture.

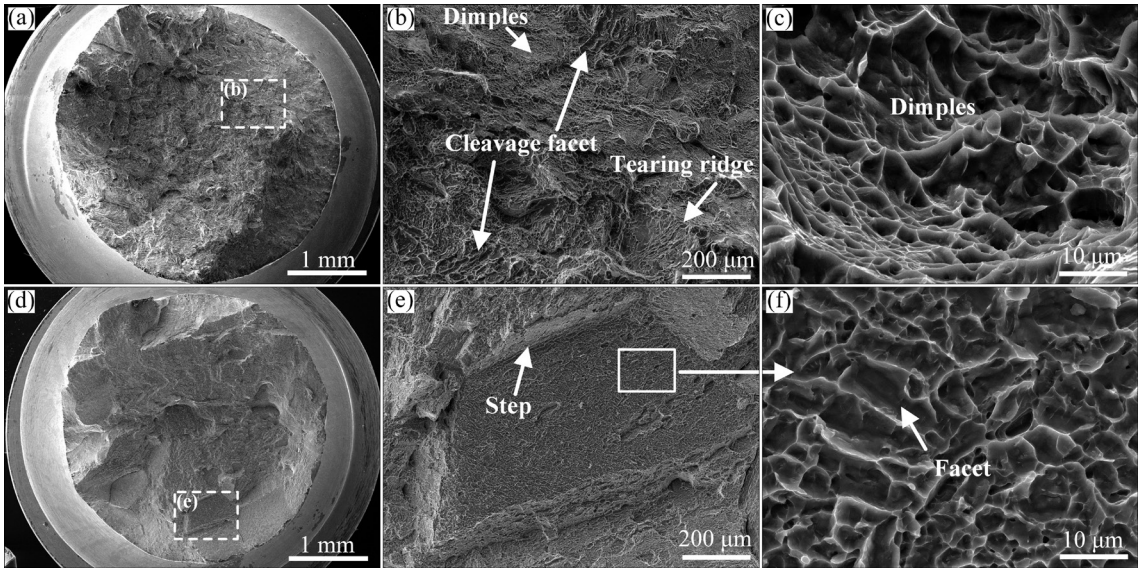

Fig. 6 Fracture surfaces of tensile specimens with different orientations: (a−c) RD specimen; (d−f) AD specimen

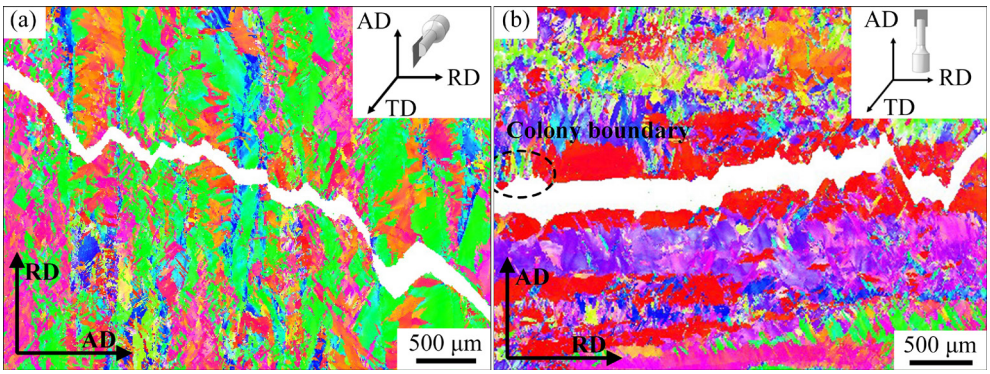

Fig. 7 Crystallographic orientation characterization of prior β grains and α colonies near crack of tensile specimens with different orientations: (a) RD specimen in AD−RD plane; (b) AD specimen in RD−AD plane

3.3 Fracture toughness

The K_Q values with different orientations are summarized in Table 3. The measured value of K_Q exceeds the plane strain requirements, indicating that the specimens are in the state of plane stress−strain mixed mode. Thus, the K_Q cannot meet the linear elastic fracture mechanics according to Eqs. (1) and (2). Table 3 also presents the thickness that meets the plane strain fracture toughness requirements. In order to obtain effective fracture toughness, a total of 17 J_{IC} values of specimens were tested. Values of J_{IC} and K_{JIC} are listed in Table 4. The J_{IC} values in RD−TD, AD−RD, and RD−AD orientations are 63, 51, and 72 kJ/m^2, respectively. Moreover, the converted value of J_{IC} to K_{IC} is K_{JIC}. The reduction equation is demonstrated in Eq. (11):

$$K_{JIC}=\sqrt{\frac{EJ_{IC}/G_{IC}}{1-\mu^2}} \tag{11}$$

Table 3 K_Q values with different orientations

Orientation	K_Q/(MPa·m$^{1/2}$)	(2.5(K_Q/YS)^2)/mm	P_Q/kN
RD−TD	102	35	57
AD−RD	98	40	56
RD−AD	120	49	68

Table 4 J_{IC}, K_{JIC}, and K_{SS} values with different orientations

Orientation	J_{IC}/(kJ·m^{-2})	K_{JIC}/(MPa·m$^{1/2}$)	K_{SS}/(MPa·m$^{1/2}$)
RD−TD	63	92	119
AD−RD	51	80	117
RD−AD	72	98	130

where G_{IC} is the strain energy release rate. E values in RD and AD are 119 and 112 GPa, respectively. The μ is selected as 0.33. After converting to K_{JIC},

the values in RD−TD, AD−RD, and RD−AD orientations are 92, 80, and 98 MPa·m$^{1/2}$, respectively. The fracture toughness of RD−AD orientation is the highest, which is 18 MPa·m$^{1/2}$ higher than that of AD−RD orientation. The K_{JIC} and K_{SS} with different orientations are presented in Fig. 8. The value of K_{SS} is the intersection of Δa=1.0 mm and J-integral curves [39], calculated by Eq. (11) for conversion. The K_{SS} values in RD−TD, AD−RD, and RD−AD orientations are 119, 117, and 130 MPa·m$^{1/2}$. Notably, the K_{JIC} and K_{SS} show the same trend. It is well known that the fracture toughness and YS of the same materials generally show an inverse trend [7,8]. Nevertheless, in this study, the fracture toughness increases with the increase of YS with different orientations. The fracture toughness of RD−AD and RD−TD corresponds to the YS of RD. The fracture toughness of AD−RD corresponds to the YS of AD. The fracture toughness of RD−AD and RD−TD is higher than that of AD−RD, and the YS of RD is higher than that of AD. Therefore, a proportional relationship exists between YS and fracture toughness. Although the trend is not apparent, it could still provide a theoretical basis for future research.

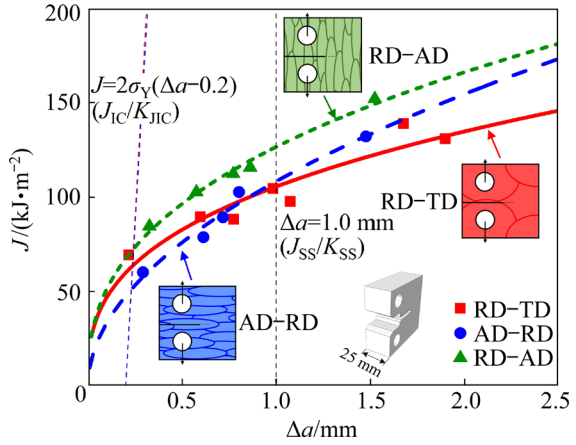

Fig. 8 J-integral fitting curves with different orientations

Fracture toughness is often used as a criterion for materials to resist crack propagation. Fracture toughness K_{IC} can also be related to the rate of strain energy release G_{IC} as indicated by Eq. (11) [40]. Both linear elastic deformation and plastic deformation exist in the material. Therefore, the following equation could be obtained according to Griffith−Orowan−Irwin theory [41]:

$$G_{IC}=2(\gamma_S+\gamma_P)=2\gamma_{eff} \tag{12}$$

where γ_S is the surface energy per unit of crack instability propagation, γ_P denotes the energy consumed by plastic deformation of the crack surface, and γ_{eff} is the unit effective surface energy. The default specimen in the equation is plane strain fracture toughness specimen, for which the plasticity at the shear lip is ignored. Moreover, previous studies also investigated the energy A_e consumed by a specific deformation in fracture, which is related to the energy γ_{eff} consumed by crack surface generation as follows:

$$A_eV=2\gamma_{eff}F \tag{13}$$

where $V\left(=\frac{\pi l}{4}hdb\right)$ is failure volume and F=hdb is the surface area of the newly created crack. l is related to the long axis of the CTPZ. The CTPZ is approximated as an ellipse, the diameter of the ellipse perpendicular to the crack is db, and the diameter parallel to the crack is h [42].

$$2\gamma_{eff}=\frac{\pi l}{4}A_e \tag{14}$$

and A_e could be obtained by the following equation:

$$A_e=\frac{(\varepsilon_u-\frac{YS}{E})(YS+UTS)}{3}+\frac{YS^2}{2E} \tag{15}$$

where ε_u is uniform elongation.

$$\begin{cases} K_{JIC}^{in}=\sqrt{\dfrac{\pi lEA_e}{4(1-\mu^2)}} \\ K_{JIC}^{ex}=\sqrt{\dfrac{\pi lEA_e}{4(1-\mu^2)}}\left(\sqrt{\dfrac{l_{(\varepsilon)}}{l_{(0)}}}-1\right) \end{cases} \tag{16}$$

where $l_{(\varepsilon)}$ is the real length of the propagation path, and $l_{(0)}$ is the characteristic constant of length.

The crack length is shown in Fig. 9. In order to accurately assess the differences among the cracks with different orientations. The crack length $l_{(\varepsilon)}$ was measured using Image Pro Plus 6. The length of $l_{(0)}$ is the horizontal length of the crack corresponding to $l_{(\varepsilon)}$. The ratios of $l_{(\varepsilon)}$ to $l_{(0)}$ in RD−TD, AD−RD, RD−AD orientations are 1.31, 1.22 and 1.35, respectively, and these differences are used to calculate quantitatively to distinguish intrinsic toughness and extrinsic toughness by Eq. (16). After the calculation, the intrinsic toughness and extrinsic toughness are shown in Table 5.

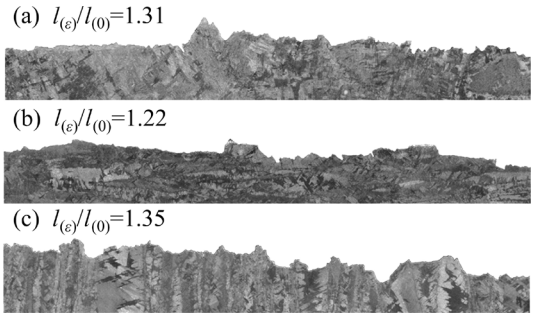

Fig. 9 Cracks zigzag degree of K_Q specimens with different orientations: (a) RD−TD specimen; (b) AD−RD specimen; (c) RD−AD specimen

Table 5 Intrinsic and extrinsic toughness with different orientations

Orientation	K_{JIC}^{in} / (MPa·m$^{1/2}$)	K_{JIC}^{ex} / (MPa·m$^{1/2}$)	Proportion of K_{JIC}^{ex} /%
RD−TD	80.4	11.6	12.6
AD−RD	72.4	7.6	9.5
RD−AD	84.4	13.6	13.9

The crack surfaces of K_Q specimens with different orientations are shown in Figs. 10(a), (c) and (e). The red dotted line in the figure indicates the zigzag degree of crack and the size of the shear lip. Consequently, the shear lip size of RD−TD and RD−AD specimens is slightly larger than that of AD−RD specimen. There is little difference between RD−TD and RD−AD in intrinsic toughness. Moreover, AD−RD exhibits a low intrinsic toughness, which is mainly controlled by the size of CTPZ, as shown in Figs. 10(b), (d) and (f). Therefore, it indicates that the elongated prior β grain morphology limits the size of CTPZ, thus reducing the intrinsic toughness of AD−RD specimen.

The extrinsic toughness of specimens is mainly controlled by the zigzag degree of crack. Therefore, the fracture morphology was studied. The fracture surfaces of K_Q specimens are shown in Fig. 11. Figures 11(a), (d) and (g) exhibit the shear lips, revealing that the specimens are in the state of plane stress−strain. Furthermore, the RD−TD specimen shows a river pattern that is parallel to the direction of crack growth. In contrast, the cleavage facets are spread over the fracture surface of AD−RD specimen, as shown in Fig. 11(e). The crack propagates preferentially along the cleavage facet [43], indicating that the resistance to crack

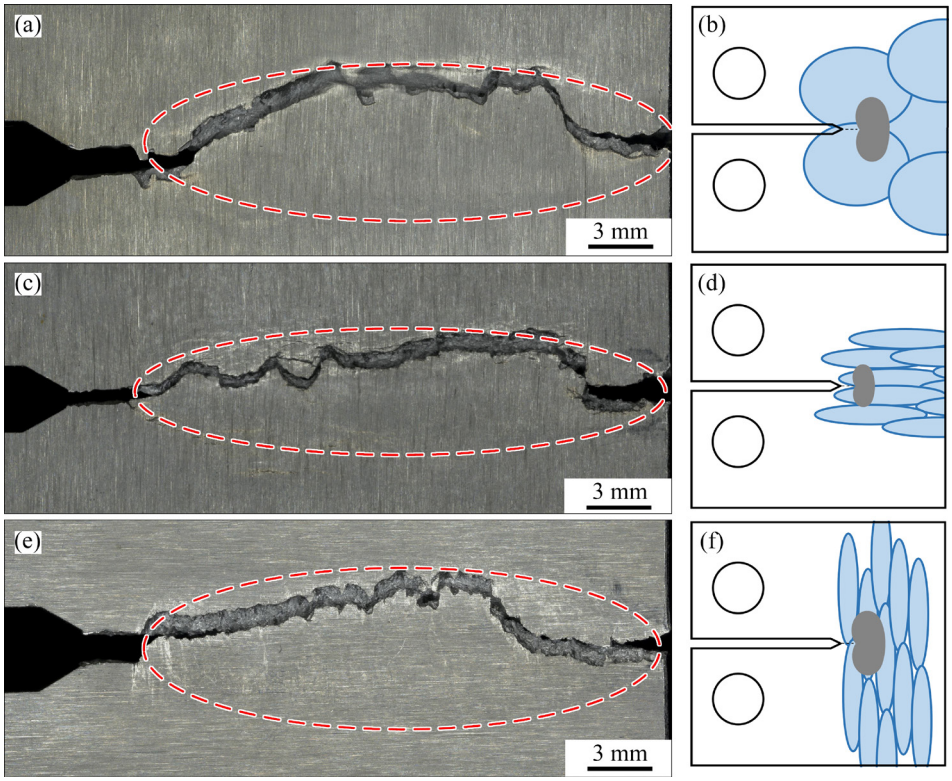

Fig. 10 Crack surfaces of K_Q specimens and schematic illustration of influence of prior β grain morphology on CTPZ size: (a, b) RD−TD specimen; (c, d) AD−RD specimen; (e, f) RD−AD specimen

propagation is smaller than that in the other two orientations. In RD−AD specimen, the river pattern perpendicular to the direction of crack propagation is observed, as shown in Figs. 11(h) and (i). At the same time, the fracture toughness of RD−AD specimen is characterized by a large amplitude of ravines with steep ups and downs, which need to consume higher energy. Moreover, the secondary cracks could be observed in RD−AD specimen, as shown in Fig. 11(i). The formation of secondary cracks requires additional energy that promotes fracture toughness [44]. In general, significant differences exist among the fracture surfaces in different orientations. The formation mechanism of cleavage facets and dimples is shown in Fig. 12. Clearly, dimples are formed when the lamellae are perpendicular to the direction of crack propagation. In contrast, the cleavage facet is formed when the lamellae are parallel to the direction of crack propagation. Therefore, as the crack propagates parallel to the long axis of elongated prior β grains in AD−RD specimen, more lamellae are parallel to the crack propagation direction, resulting in massive cleavage facets.

Furthermore, the macroscopic zigzag degree of cracks was analyzed. In ductile metallic materials with lamellar structures, fracture toughness is enhanced due to cracks propagating in deflection,

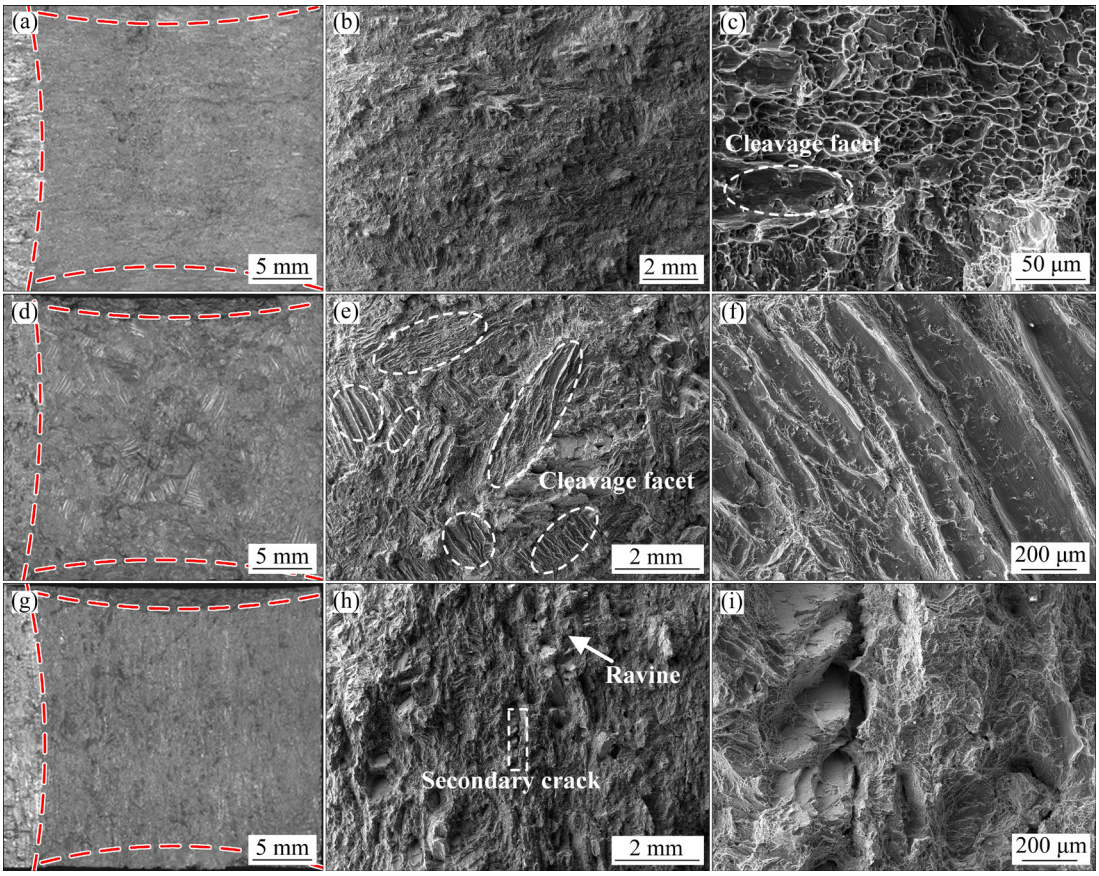

Fig. 11 Fracture surfaces of K_Q specimens with different orientations: (a−c) RD−TD specimen; (d−f) AD−RD specimen; (g−i) RD−AD specimen

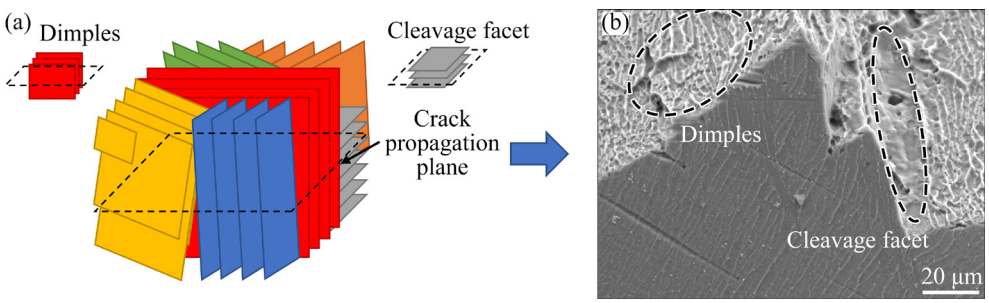

Fig. 12 Schematic illustration showing formation (a) and SEM image (b) of cleavage facet and dimples

branching, bridging, and delamination [12]. As mentioned previously, most of the cracks propagate parallel to α and β lamellae, occasionally along the grain boundary α [43]. Figures 13(a), (c) and (e) show the prior β grain morphology during crack propagation in different orientations. As shown in Figs. 13(b), (d) and (f), the direction of crack propagation is deflected with different angles of lamellae, and presents a small scale deflection. Figures 13(b) and (f) show the voids nucleation and crack propagation in RD−TD and RD−AD orientations. Owing to the inconsistency of the hardness between the α phase and the β phase, the strain inhomogeneity between the precipitated α lamellae and the β lamellae leads to interfacial plastic incompatibility, resulting in micro-voids [45] and secondary cracks near the main cracks. When the crack propagates through the void and secondary crack, the zigzag degree of the crack and the energy dissipation of the crack propagation increase. Figures 13(b) and (f) illustrate that secondary cracks and voids are easily generated in the α phase matrix and propagate parallel to the lamellar β phase. Furthermore, the prior β grain boundaries (or β lamellae) in AD−RD specimen are parallel to the orientation of crack propagation, as shown in Fig. 13(d), which leads to the formation of the cleavage facet, thus reducing the zigzag degree of cracks. Figures 13(e) and (f) demonstrate that the elongated prior β grains are perpendicular to the direction of crack propagation, and the cracks pass through more prior β grains during the process of crack propagation. However, most of the cracks do not deviate during the crack crossing the prior β

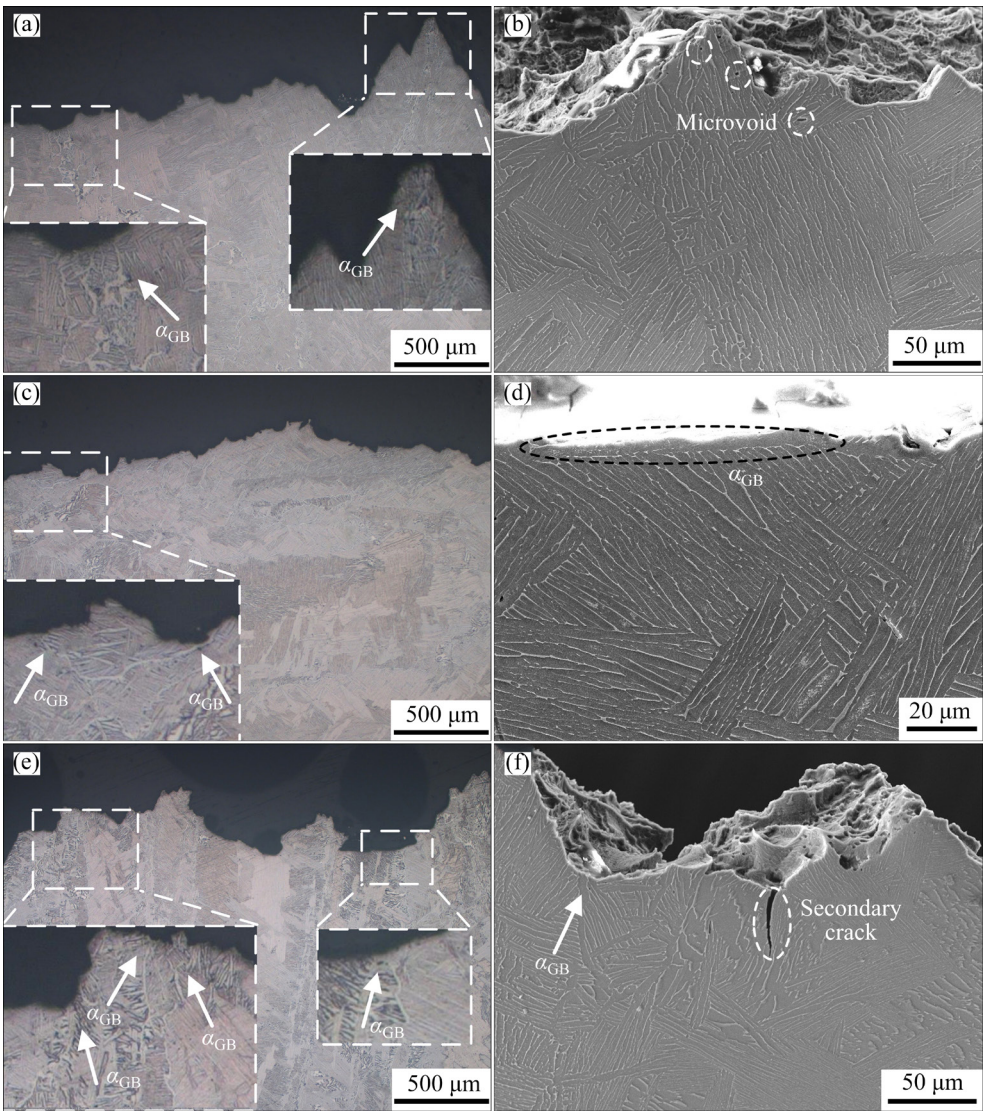

Fig. 13 Crack propagation paths of K_Q specimens with different orientations: (a, b) RD−TD specimen; (c, d) AD−RD specimen; (e, f) RD−AD specimen

grain boundaries as shown in Figs. 13(a), (c) and (e), and only a few cracks propagate along the β lamellae at a small distance during the crack crossing the prior β grain boundaries. The colonies formed by plenty of orderly lamellae arrangements strongly affect the inhibition of cracks than prior β grain boundaries. Therefore, the larger zigzag degree of cracks in RD−AD specimen can be attributed to the influence of different colonies [9,10] on its deflection, as shown in Figs. 13(e) and (f) and Fig. 14(c), and this phenomenon leads to delamination, which increases extrinsic toughness.

Furthermore, Figs. 14(a) and (b) demonstrate that the crystal orientation of colonies has almost no effect on the crack zigzag degree of RD−TD and AD−RD specimens. The crack is deflected by colonies of different crystal orientations for RD−AD specimen. Moreover, Fig. 14(c) exhibits that the intensity of α texture in forged billet is low, which results in the small effect of α texture on the anisotropy of fracture toughness.

4 Conclusions

(1) The intensity of prior β texture in Ti64 billet manufactured by β forging is high in single phase region. However, the intensity of α texture is lower at ambient temperature, which is attributed to a large number of α phases precipitated inside the prior β grains without variant selection. Only a part of α phases at grain boundaries undergo variant selection and inherit a small portion of the prior β texture.

(2) The anisotropic tensile properties are affected by elongated prior β grains and α texture. The elongated prior β grains of the cross-section

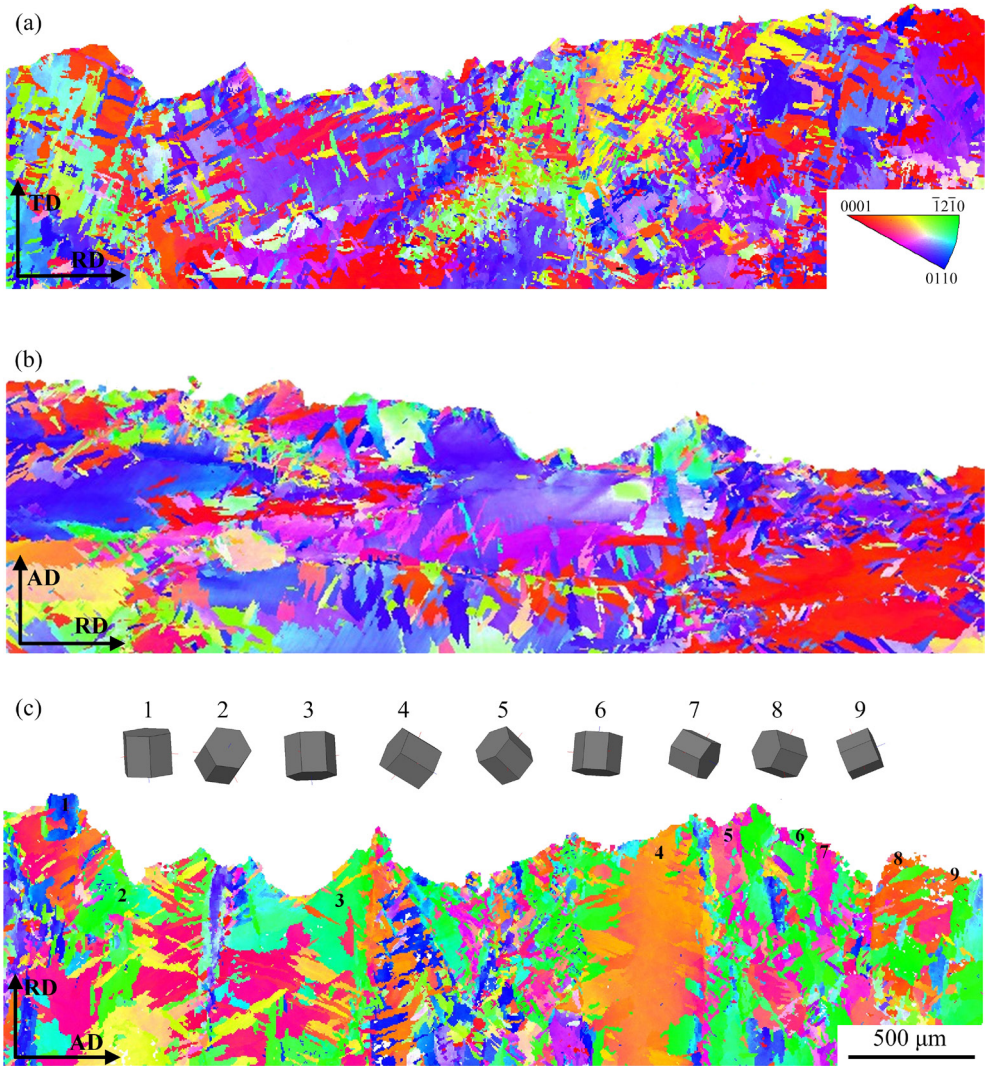

Fig. 14 Crystallographic orientation characterization of prior β grains and α colonies near crack of K_Q specimens with different orientations: (a) RD−TD specimen; (b) AD−RD specimen; (c) RD−AD specimen

parallel to the fracture surface increase the yield strength of the radial direction specimens relative to axial direction. The α texture of $\langle 11\bar{2}0\rangle$//AD increases the probability of prismatic slip and reduces the yield strength of AD specimens. However, the normal stress perpendicular to the long axis of the prior β grains makes the crack propagate horizontally in AD specimens, thus reducing the elongation of AD specimens.

(3) The initiation toughness of different orientations was subdivided into intrinsic and extrinsic toughness by calculation. The intrinsic toughness of anisotropy is attributed to the effect of prior β grain morphology on the size of the crack tip plastic zone, while the anisotropic extrinsic toughness is related to the influence of α colonies on zigzag degree of cracks.

Acknowledgments

This work was supported by the Strategic Priority Research Program of the Chinese Academy of Sciences (No. XDA22010101), the National Natural Science Foundation of China (No. 51871225), the National Key Research and Development Program of China (No. 2021YFC2801800), and the Youth Innovation Promotion Association CAS and Liaoning Revitalization Talents Program, China (No. XLYC1907005).

References

[1] OBERWINKLER B, RIEDLE R M, EICHLSEDER W. Importance of local microstructure for damage tolerant light weight design of Ti−6Al−4V forgings [J]. International Journal of Fatigue, 2010, 32(5): 808−814.

[2] SESHACHARYULU T, MEDEIROS S C, FRAZIER W G, PRASAD Y V R K. Microstructural mechanisms during hot working of commercial grade Ti−6Al−4V with lamellar starting structure [J]. Materials Science and Engineering: A, 2002, 325(1/2): 112−125.

[3] BANERJEE D, WILLIAMS J C. Perspectives on titanium science and technology [J]. Acta Materialia, 2013, 61(3): 844−879.

[4] SUN Hong, YU Li-ming, LIU Yong-chang, ZHANG Li-ye, LIU Chen-xi, LI Hui-jun, WU Jie-feng. Effect of heat treatment processing on microstructure and tensile properties of Ti−6Al−4V−10Nb alloy [J]. Transactions of Nonferrous Metals Society of China, 2019, 29(1): 59−66.

[5] ZHAO Yong-qing, QU Heng-lei. Research on high strength and high toughness titanium alloy with damage tolerance [J]. Materials Science Forum, 2010, 654/655/656: 586−589.

[6] SHI Zhi-feng, GUO Hong-zhen, ZHANG Jian-wei, YIN Jian-ning. Microstructure fracture toughness relationships and toughening mechanism of TC21 titanium alloy with lamellar microstructure [J]. Transactions of Nonferrous Metals Society of China, 2018, 28(12): 2440−2448.

[7] XU Jian-wei, ZENG Wei-dong, ZHOU Da-di, MA Hao-yuan, CHEN Wei, HE Sheng-tong. Influence of alpha/beta processing on fracture toughness for a two-phase titanium alloy [J]. Materials Science and Engineering: A, 2018, 731: 85−92.

[8] LEI Zhen-ni, GAO Peng-fei, LI Hong-wei, CAI Yang, ZHAN Mei. On the fracture behavior and toughness of TA15 titanium alloy with tri-modal microstructure [J]. Materials Science and Engineering: A, 2019, 753: 238−246.

[9] WEN Xin, WAN Ming-pan, HUANG Chao-wen, LEI Min. Strength and fracture toughness of TC21 alloy with multi-level lamellar microstructure [J]. Materials Science and Engineering: A, 2019, 740/741: 121−129.

[10] WEN Xin, WAN Ming-pan, HUANG Chao-wen, TAN Yuan-biao, LEI Min, LIANG Yi-long, CAI Xin. Effect of microstructure on tensile properties, impact toughness and fracture toughness of TC21 alloy [J]. Materials & Design, 2019, 180: 107898.

[11] WU Chuan, ZHAN Mei. Microstructural evolution, mechanical properties and fracture toughness of near β titanium alloy during different solution plus aging heat treatments [J]. Journal of Alloys and Compounds, 2019, 805: 1144−1160.

[12] ZHU Wen-guang, LEI Jia, SU Bin, SUN Qiao-yan. The interdependence of microstructure, strength and fracture toughness in a novel β titanium alloy Ti−5Al−4Zr−8Mo−7V [J]. Materials Science and Engineering: A, 2020, 782: 139248.

[13] MEYN D A. Effect of hydrogen on fracture and inert-environment sustained load cracking resistance of α/β titanium alloys [J]. Metallurgical and Materials Transactions B, 1974, 5(11): 2405−2414.

[14] CHEN Fu-wen, GU Yu-lei, XU Guang-long, CUI Yu-wen, CHANG Hui, ZHOU Lian. Improved fracture toughness by microalloying of Fe in Ti−6Al−4V [J]. Materials & Design, 2020, 185: 108251.

[15] AN Fei-peng, ZHANG Bin-bin, YAN Yang-yang, WANG Lin. Effect of vanadium contents on microstructure and mechanical properties of Ti−6Al−xV components produced by wire + arc additive manufacturing [J]. Materials Transactions, 2021, 62(8): 1071−1078.

[16] TCHORZEWSKI R M, HUTCHINSON W B. Anisotropy of fracture toughness in textured Ti−6Al−4V alloy [J]. Metallurgical Transactions A, 1978, 9(8): 1113−1124.

[17] HELBERT A L, FEAUGAS X, CLAVEL M. The influence of internal stresses on the fracture toughness of α/β titanium alloys [J]. Metallurgical and Materials Transactions A, 1999, 30(11): 2853−2863.

[18] HELBERT A L, FEAUGAS X, CLAVEL M. Effects of microstructural parameters and back stress on damage mechanisms in α/β titanium alloys [J]. Acta Materialia, 1998, 46(3): 939−951.

[19] HELBERT A L, FEAUGAS X, CLAVEL M. The influence

of stress triaxiality on the damage mechanisms in an equiaxed α/β Ti−6Al−4V alloy [J]. Metallurgical and Materials Transactions A, 1996, 27(10): 3043−3058.

[20] BOWEN A W. The influence of crystallographic orientation on the fracture toughness of strongly textured Ti−6Al−4V [J]. Acta Metallurgica, 1978, 26(9): 1423−1433.

[21] PENG Xiao-na, GUO Hong-zhen, WANG Tao, YAO Ze-kun. Effects of β treatments on microstructures and mechanical properties of TC4-DT titanium alloy [J]. Materials Science and Engineering: A, 2012, 533: 55−63.

[22] CVIJOVIĆ-ALAGIĆ I, GUBELJAK N, RAKIN M, CVIJOVIĆ Z, GERIĆ K. Microstructural morphology effects on fracture resistance and crack tip strain distribution in Ti−6Al−4V alloy for orthopedic implants [J]. Materials & Design, 2014, 53: 870−880.

[23] FILIP R, KUBIAK K, ZIAJA W, SIENIAWSKI J. The effect of microstructure on the mechanical properties of two-phase titanium alloys [J]. Journal of Materials Processing Technology, 2003, 133(1/2): 84−89.

[24] ZHANG Kun, ZHANG Kai, ZHU Yu-man, WU Xin-hua, WILLIAMS J, LIANG En-quan, MA Ji-sheng, ZHANG Ren, LIM C V S, HUANG Ai-jun. Effect of deformation reduction on microstructure, texture, and mechanical properties of forged Ti−6Al−4V [J]. Journal of Materials Engineering and Performance, 2021, 30(2): 1147−1156.

[25] MENG L, KITASHIMA T, TSUCHIYAMA T, WATANABE M. β-texture evolution of a near-β titanium alloy during cooling after forging in the β single-phase and $(\alpha+\beta)$ dual-phase regions [J]. Metallurgical and Materials Transactions A, 2021, 52(1): 303−315.

[26] CHEN Wei, ZENG Wei-dong, ZHAO Yao-hua, GAO Pan, XU Jian-wei, ZHAO Qin-yang. Fracture toughness anisotropy of Ti17 billet processed by the β forging [J]. Materials Science and Engineering: A, 2021, 807: 140825.

[27] RITCHIE R O. The conflicts between strength and toughness [J]. Nature Materials, 2011, 10(11): 817−822.

[28] RITCHIE R O. Mechanisms of fatigue crack propagation in metals, ceramics and composites: Role of crack tip shielding [J]. Materials Science and Engineering: A, 1988, 103(1): 15−28.

[29] COLLINS P C, KODURI S, DIXIT V, FRASER H L. Understanding the interdependencies between composition, microstructure, and continuum variables and their influence on the fracture toughness of α/β-processed Ti−6Al−4V [J]. Metallurgical and Materials Transactions A, 2018, 49(3): 848−863.

[30] HE Sheng-tong, ZENG Wei-dong, XU Jian-wei, CHEN Wei. The effects of microstructure evolution on the fracture toughness of BT-25 titanium alloy during isothermal forging and subsequent heat treatment [J]. Materials Science and Engineering: A, 2019, 745: 203−211.

[31] SHI Xiao-hui, ZENG Wei-dong, SHI Chun-ling, WANG Hao-jun, JIA Zhi-qiang. The fracture toughness and its prediction model for Ti−5Al−5Mo−5V−1Cr−1Fe titanium alloy with basket-weave microstructure [J]. Journal of Alloys and Compounds, 2015, 632: 748−755.

[32] ZHU Xian-kui, JOYCE J A. Review of fracture toughness (G, K, J, CTOD, CTOA) testing and standardization [J]. Engineering Fracture Mechanics, 2012, 85: 1−46.

[33] ASTM Standard E399, Standard test method for linear-elastic plane-strain fracture toughness K_{IC} of metallic materials [S]. 2017.

[34] ASTM Standard E1820, Standard test method for measurement of fracture toughness [S]. 2019.

[35] STANFORD N, BATE P S. Crystallographic variant selection in Ti−6Al−4V [J]. Acta Materialia, 2004, 52(17): 5215−5224.

[36] BACHMANN F, HIELSCHER R, SCHAEBEN H. Texture analysis with MTEX-free and open source software toolbox [J]. Solid State Phenomena, 2010, 160: 63−68.

[37] LÜTJERING G, ALBRECHT J, SAUER C, KRULL T. The influence of soft, precipitate-free zones at grain boundaries in Ti and Al alloys on their fatigue and fracture behavior [J]. Materials Science and Engineering: A, 2007, 468/469/470: 201−209.

[38] LEI Lei, ZHAO Yong-qing, ZHAO Qin-yang, WU Cong, HUANG Shi-xing, JIA Wei-ju, ZENG Wei-dong. Impact toughness and deformation modes of Ti−6Al−4V alloy with different microstructures [J]. Materials Science and Engineering: A, 2021, 801: 140411.

[39] CAO Ru-qing, YU Qin, PAN Jie, LIN Yan, SWEET A, LI Yi, RITCHIE R O. On the exceptional damage-tolerance of gradient metallic materials [J]. Materials Today, 2020, 32: 94−107.

[40] RAGOZIN Y I, ANTONOV Y. Method of accelerated fracture toughness K_{IC} testing of metallic materials [J]. Strength of Materials, 1984, 16(2): 179−184.

[41] MAKHUTOV N A, MATVIENKO Y G. Griffith theory and development of fracture mechanics criteria [J]. Materials Science, 1993, 29(3): 316−319.

[42] ZHANG Peng-hui, ZENG Wei-dong, ZHENG You-ping, XU Jian-wei, LIANG Xiao-bo, ZHAO Yong-qing. Fracture toughness of Ti−22Al−25Nb alloy at room and high temperatures [J]. Materials Science and Engineering: A, 2020, 796: 140009.

[43] ZHENG You-ping, ZENG Wei-dong, LI Dong, MA Hao-yuan, ZHANG Peng-hui, MA Xiong. Quasi cleavage fracture of the bimodal size lamellar O phase microstructure of a Ti_2AlNb based alloy [J]. Journal of Alloys and Compounds, 2019, 799: 267−278.

[44] FAN J K, LI Jin-shan, KOU Hong-chao, HUA Ke, TANG Bin. The interrelationship of fracture toughness and microstructure in a new near β titanium alloy Ti−7Mo−3Nb−3Cr−3Al [J]. Materials Characterization, 2014, 96: 93−99.

[45] ASHBY M F. The deformation of plastically non-homogeneous materials [J]. Journal of Theoretical Experimental and Applied Physics, 1970, 21(170): 399−424.

β锻造 Ti−6Al−4V 合金力学性能各向异性

翁涵博[1,2]，黄森森[2]，杨 杰[2,3]，齐 敏[2,3]，马英杰[2,3]，
王宇翔[2]，许道奎[2,3]，邱建科[2,3]，雷家峰[2,3]，龚 斌[1]，杨 锐[2,3]

1. 沈阳化工大学 机械与动力工程学院，沈阳 110142；
2. 中国科学院 金属研究所 师昌绪先进材料创新中心，沈阳 110016；
3. 中国科学技术大学 材料科学与工程学院，沈阳 110016

摘 要：研究 β 锻造 Ti−6Al−4V(Ti64)合金拉伸性能和断裂韧性的各向异性。对饼材不同取向的显微组织和晶体学织构进行分析，同时研究取样方向对拉伸性能、断裂韧性的影响。结果表明，Ti64 饼材原始 β 晶粒呈扁平状。室温下合金主要由 α 相构成，β 锻造后 β→α 相变产生的多个 α 相变体导致 α 相织构强度较低。力学性能各向异性的主要影响因素为原始 β 晶粒形貌以及与 α 织构相关的滑移。采用 *J* 积分阻力曲线法测定合金的起裂韧性，并将起裂韧性 K_{JIC} 分为内在韧性和外在韧性。内在断裂韧性各向异性主要与原始 β 晶粒对裂纹尖端塑性区范围的影响相关；外在断裂韧性主要与 α 片层与集束对裂纹曲折程度的影响相关。

关键词：钛合金；β 锻造；织构；*J* 积分；断裂机理；各向异性

(Edited by Wei-ping CHEN)